

Document Version

Final published version

Licence

CC BY

Citation (APA)

Kramer, O. J. I., van Schaik, C., Hangelbroek, J. J., de Moel, P. J., Colin, M. G., Amsing, M., Boek, E. S., Breugem, W. P., Padding, J. T., & van der Hoek, J. P. (2021). A novel sensor measuring local voidage profile inside a fluidised bed reactor. *Journal of Water Process Engineering*, 42, Article 102091. <https://doi.org/10.1016/j.jwpe.2021.102091>

Important note

To cite this publication, please use the final published version (if applicable).
Please check the document version above.

Copyright

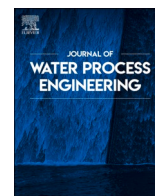
In case the licence states "Dutch Copyright Act (Article 25fa)", this publication was made available Green Open Access via the TU Delft Institutional Repository pursuant to Dutch Copyright Act (Article 25fa, the Taverne amendment). This provision does not affect copyright ownership.
Unless copyright is transferred by contract or statute, it remains with the copyright holder.

Sharing and reuse

Other than for strictly personal use, it is not permitted to download, forward or distribute the text or part of it, without the consent of the author(s) and/or copyright holder(s), unless the work is under an open content license such as Creative Commons.

Takedown policy

Please contact us and provide details if you believe this document breaches copyrights.
We will remove access to the work immediately and investigate your claim.



A novel sensor measuring local voidage profile inside a fluidised bed reactor

O.J.I. Kramer^{a,b,c,d,g,*}, C. van Schaik^{c,d}, J.J. Hangelbroek^c, P.J. de Moel^{a,c,e}, M.G. Colin^c, M. Amsing^f, E.S. Boek^g, W.P. Breugem^b, J.T. Padding^b, J.P. van der Hoek^{a,c}

^a Delft University of Technology, Faculty of Civil Engineering and Geosciences, Department of Water Management, PO Box 5048, 2600 GA, Delft, the Netherlands

^b Delft University of Technology, Faculty of Mechanical, Maritime and Materials Engineering, Department of Process and Energy, Leeghwaterstraat 39, 2628 CB, Delft, the Netherlands

^c Waternet, PO Box 94370, 1090 GJ, Amsterdam, the Netherlands

^d HU University of Applied Sciences Utrecht, Institute for Life Science and Chemistry, PO Box 12011, 3501 AA, Utrecht, the Netherlands

^e Omnisys, Eiberlaan 23, 3871 TG, Hoevelaken, the Netherlands

^f Bienfait, Waarderweg 54, 2031 BP, Haarlem, the Netherlands

^g Queen Mary University of London, Division of Chemical Engineering, School of Engineering and Materials Science, Mile End Road, London, E1 4NS, United Kingdom

ARTICLE INFO

Keywords:

Fluidization
Drinking water treatment
Pellet-softening
Hydrostatic soft sensor
Hydraulic state

ABSTRACT

Liquid-solid fluidisation is frequently encountered in drinking water treatment processes, often to obtain a large liquid-solid interfacial surface area. A large surface area is crucial for optimal seeded crystallisation in full-scale softening reactors. Due to crystallisation, particles grow and migrate to a lower zone in the reactor which leads to a stratified bed. Larger particles adversely affect the surface area. To maintain optimal process conditions in the fluidised beds, information is needed about the distribution of particle size, local voidage and available surface area, over the reactor height.

In this work, a sensor is developed to obtain the hydraulic state gradient, based on *Archimedes'* principle. A cylindrical heavy object is submerged in the fluidised bed and lowered gradually while its weight is measured at various heights using a sensitive force measuring device.

Based on accurate fluidisation experiments with calcite grains, the voidage is determined and a straightforward empirical model is developed to estimate the particle size as a function of superficial fluid velocity, kinematic viscosity, suspension density, voidage and particle density. The surface area and specific space velocity can be estimated accordingly, which represent key performance indicators regarding the hydraulic state of the fluidised bed reactor. The prediction error for voidage is $5 \pm 2\%$ and for particle size $9 \pm 4\%$.

The newly developed soft sensor is a more time-effective method for obtaining the hydraulic state in full-scale liquid-solid fluidised bed reactors.

Abbreviations: ARE, average relative error; CCCP, calcium carbonate crystallisation potential; CC, crushed calcite; CO, cylindrical object; CP, calcite pellets; DTM, data transformation model; GB, glass beads; KPI, key performance indicators; LSF, liquid-solid fluidisation; DTM, data-transformation-model; SSA, specific crystallisation surface area; SSV, specific space velocity; TSA, total surface area.

* Corresponding author at: Delft University of Technology, Faculty of Civil Engineering and Geosciences, Department of Water Management, PO Box 5048, 2600 GA, Delft, the Netherlands.

E-mail addresses: o.j.i.kramer@tudelft.nl, onno.kramer@waternet.nl (O.J.I. Kramer), e.boek@qmul.ac.uk (E.S. Boek).

<https://doi.org/10.1016/j.jwpe.2021.102091>

Received 12 March 2021; Received in revised form 12 April 2021; Accepted 15 April 2021

Available online 2 June 2021

2214-7144/© 2021 The Author(s). Published by Elsevier Ltd. This is an open access article under the CC BY license (<http://creativecommons.org/licenses/by/4.0/>).

Nomenclature			
A_1	Surface area of one spherical particle [m ²]	N_p	Total number of particles [#]
A_c	Specific space velocity [s ⁻¹]	N_r	Number of reactors [#]
A_i	Projected particle area using static image analysis [m ²]	$\Delta P/L$	Pressure drop head loss [kPa/m]
$A_{s,r}$	Specific surface area (reactor) [m ² /m ³]	ΔP_{max}	Total maximum differential pressure over the bed [kPa]
$A_{s,w}$	Specific surface area (water) [m ² /m ³]	Q_w	Water flow [m ³ /h]
A_{\perp}	Cross sectional area of the object perpendicular to the flow [m ²]	Re_p	Reynolds particle number [-]
c_i	Coefficients [-]	Re_t	Reynolds terminal number [-]
C_w	Drag coefficient [-]	S	Strain / stress [V]
D	Inner column or cylinder vessel diameter [m]	St	Stokes number [-]
D_{co}	Diameter cylindrical object [m]	t_f	Fluid response [s]
D_{hm}	Inner column diameter hydrometer [m]	t_p	Particle response [s]
d_p	Effective or average or particle equivalent diameter [m]	T	Temperature [°C]
Δd_p	Distance between the centres of two spherical particles [m]	v_i	Interstitial fluid velocity or phase-averaged bulk fluid velocity [m/s]
d_i	Effective size of a sample where i percentage of particles is smaller than the particular size [m]	v_s	Linear superficial velocity or empty tube fluidisation velocity [m/s]
$d_{s,i}$	Sieve mesh diameter [m]	V	Volume [m ³]
E	Bed expansion [%]	V_{object}	Object volume [m ³]
f_c	Correction factor [-]	W	Weight of object in air [N]
F_b	Buoyancy force [N]	W_{sub}	Weight of submerged object in water [N]
F_{col}	Force caused by particle collisions [N]	z	Height [m]
F_d	Drag force [N]		
F_g	Gravitational force [N]	Greek symbols	
F_s	Upward strain force [N]	α	Linear heat expansion coefficient [m/mK]
Fr_p	Densimetric or particle Froude number [-]	ϵ	Voidage or voidage of the system [m ³ /m ³]
g	Local gravitational field of earth equivalent to the free-fall acceleration [m/s ²]	ϵ_0	Fixed bed voidage [-]
ΔL	Relative total fluid bed height [m]	ϵ_1	Voidage at situation 1 (with no distorted bed) [-]
L	Fluid bed height [m]	ϵ_2	Voidage at situation 2 (due to constriction caused by the object in the bed) [-]
L_0	Fixed bed height [m]	ϵ_{mf}	Voidage at minimum fluidisation [-]
m_g	Object mass (in air) [kg]	η	Dynamic fluid viscosity [kg/(m s)]
m_i	Single particle mass [kg]	η_{mix}	Dynamic viscosity of mixture [kg/(m s)]
m	Total particle mass [kg]	ρ_{co}	Density cylindrical object [kg/m ³]
m_{strain}	Object mass apparent (mass while submerged in fluidised bed) [kg]	ρ_f	Fluid density [kg/m ³]
m_{sub}	Submerged object mass (in water) [kg]	ρ_{mix}	Suspension density (particles and fluid) [kg/m ³]
N	Total number experiments [#]	ρ_p	Particle density [kg/m ³]
		Φ	Sphericity: ratio between surface area of the volume equivalent sphere and considered particle [-]

Table 5. Dimensionless numbers.

Number	Equation	Equation number
Reynolds tube	$Re = \frac{\rho_f v_s D}{\eta}$	(25)
Reynolds cylinder	$Re_{co} = \frac{\rho_f v_s D_{co}}{\eta}$	(26)
Stokes	$St = \frac{g d_p^2}{18 \eta}$	(27)
Reynolds particle	$Re_p = \frac{\rho_f d_p v_s}{\eta}$	(28)
Densimetric particle Froude	$Fr_p = \frac{v_s}{\sqrt{\left(\frac{\rho_p}{\rho_f} - 1\right) g d_p}}$	(10)

1. Introduction

1.1. Liquid-solid fluidisation applied in drinking water softening processes

Liquid-solid fluidisation is a commonly applied process in drinking water treatment processes, often to effectuate a large liquid-solid interfacial surface area [1]. In particular, pellet softening, a process based on seeded crystallisation in fluidised bed reactors, requires a large surface area for crystallisation purposes [2]. Water softening is a frequently applied treatment step in drinking water treatment [3]. The

removal of dissolved calcium from the water has benefits for public health, environment, economy and aesthetics. In addition, it counteracts limescale [4]. In the Netherlands, more than 400 million m³ water is softened annually in drinking water treatment plants using fluidised bed pellet reactors [5]. In these reactors, sand is traditionally dosed as seeding material. Calcite pellets are produced as a by-product [6]. To meet sustainability goals, calcite pellets are dried, grained, sieved and re-used as seeding material [7]. By carefully dosing caustic soda, supersaturated conditions are created in the fluidised bed [8], leading to calcium carbonate crystallisation on the surface of calcite grains. Crystallisation causes particles to grow and to migrate to a lower region in the reactor which leads to a stratified bed and a certain particle size profile (0.2–2.0 mm) from top to bottom of the bed. Larger particles reduce the available surface area which adversely affects the crystallisation efficiency. In addition, too large calcite pellets may cause detrimental clogging at the bottom of the reactor, due to a highly alkaline environment caused by caustic soda dosage if the superficial fluid velocity approaches the minimum fluidisation state. Therefore, when a certain particle size threshold is exceeded, calcite pellets are extracted from the bottom of the reactors. To maintain optimal process conditions *i.e.* fast calcium carbonate crystallisation in the fluidised beds, information is needed about particle size, local voidage and specific surface area (SSA), over the reactor height [9].



Fig. 1. Full-scale pellet softening reactors located at Waternet (Amsterdam, The Netherlands) [10].

In full-scale industrial pellet-softening reactors (Fig. 1), the condition of the fluidised bed is not available to the operator in real-time. To obtain direct particle information, on a frequent basis, laborious manual action is necessary, such as particle sampling from the reactor bed, using hoses that might be hazardous in terms of water quality *i.e.* hygiene requirements [11]. Moreover, particle samples must be dried, weighed, sieved and analysed accordingly, which is time consuming, expensive, and only provides delayed information about a small section of the reactor.

Indirect fluidised bed information can also be acquired using online sensors [12]. The total pressure drop and bed height can be used to estimate the total average bed voidage. More advanced methods are also applied on a reactor equipped with a differential pressure measurement sensor between heights of 15 and 65 cm in the reactor [13]. Using the fact that the hydraulic pressure drop must be equal to the submerged weight of the suspended bed material per unit cross-sectional area, the local voidage in the reactor zone with the highest supersaturation driving force can be estimated. Using hydraulic models such as Ergun [14], Carman–Kozeny [15] or van Dijk [6], the local average particle size can be estimated [16]. Knowing these values is operationally beneficial for determining effectivity, and the point at which particles need to be removed. However, the information received is averaged, and does not provide a complete description of the hydraulic state.

1.2. Hydraulic state determination of pellet-softening fluidised beds

Due to seasonal changes, surface water temperature in the Netherlands changes throughout the year between 1 and 20 °C. This affects the degree of fluidised bed expansion in pellet-softening reactors. To maintain optimal process conditions for calcium carbonate crystallisation, sufficient particle surface area must be retained in the fluidised bed. Moreover, through a transition from garnet sand as a seeding material, to a more sustainable re-use of crushed calcite pellets [7,9], particle properties of calcite particles have changed. A consequence, however, is that particle size and shape of these granules affect the condition and performance of the distinct unit-operation, causing an altering degree of expansion and a risk of particle flushing. In addition, when calcite pellet erosion occurs, with high turbidity as a result in the water phase, the bed height sensor often cannot detect the bed height.

In practice, it is rather complex to comprehend the overall seeded crystallisation softening process that occurs in a stratified bed with a variety of large spherical and small highly non-spherical particles with different hydraulic behaviour. For this reason, operators have to build up significant experience in operations and often use "rules of thumb" [17] and experience to control and optimise the process [10,5,18]. Additional full-scale considerations to operations can be found in the

Supplementary material (Section 6).

Up to this point, it has not been possible to fully determine the real time dynamics of the fluidised bed from the outside of a reactor or based on overall process variables such as water temperature, flow, bed height and total differential pressure. The pellet-softening process has proven to be complex and it is not completely understood if multiplicity *i.e.* multiple process states occur.

For safe water production [19] and optimal process conditions, a more flexible process control is needed [20]. With regard to pellet-softening this means that an improvement is needed for fast, on-line determination of the hydraulic state of the fluidised bed in pellet-softening reactors.

The objective of this work is to experimentally measure the force acting on a submerged object in a liquid-solid fluidised bed and use this information to determine the suspension density and voidage along the bed height. The voidage measurement is based on *Archimedes'* principle, and is compared with the measured bed height and mass-based mean voidage. The overall aim of this research is to test the novel developed sensor to obtain longitudinal information of the hydraulic state gradient in a drinking water pellet-softening reactor, where chemistry and hydraulics are inextricably interlinked.

The approach in this work is a feasibility study to demonstrate that the *Archimedes*-based novel sensor, termed as 'the Hydrometer', works in a liquid-solid fluidised bed reactor.

First, an overview is given of the existing scientific literature about submerged objects in fluidised beds and its applications. To explore the existence of a weight gradient, a preliminary trial was carried out in a full-scale reactor. An advanced experimental set-up was been designed and constructed to investigate the possibility of measuring the weight changes of a submerged object for various heights in the fluidised bed.

The novelty of this work lies in the combination of classical physics *i.e.* *Archimedes'* principle and the translation into particle properties which serves as a semi-online sensor to determine the hydraulic state of a liquid-solid fluidised bed reactor.

2. Materials and methods

Experiments are executed in the experimental set-up with glass beads to scrutinise the dimensions of the submerged objects. A series of experiments are performed with a mixture of two sets of fractionised calcite grains from a pellet-softening reactor to investigate the possibility to distinguish the transition from one layer to another when the object is gradually lowered. Furthermore, two single fractions of calcite pellets are used to examine whether the spherically-assumed particle size can be predicted using a novel data-driven model based on the known particle and fluid properties. A sensibility analysis is conducted

to determine the implications for the data conversion steps *i.e.* the data-transformation-model (DTM). Additionally, key performance indicators (KPI) are presented to assess the hydraulic reactor performance. Finally, the practical utility in full-scale operation is discussed.

2.1. Experimental set-up

An experimental set-up was designed at Waternet and at the University of Applied Sciences Utrecht, the Netherlands (Fig. 3). A transparent 2 m cylindrical PVC column (Fig. 4) with an inner diameter of 123 mm was used for the fluidisation experiments. The bottom section of the column was equipped with a membrane with a mesh of 120 μm ; this membrane functioned as the base of the bed. The purpose of the membrane distributor was to allow water to flow through the bed with a uniform velocity profile across the bed cross section, thereby preventing inhomogeneities. Locally produced drinking water was used for the experiments. An overflow at the top of the column was used to recirculate the water through a buffer vessel and a reservoir. The column was mounted in an aluminium frame to accommodate the measuring apparatus and ensure a levelled column. A centrifugal pump with valves created an adjustable upward flow that was measured by a calibrated flow meter. The flow rate entering the system could be controlled through opening and closing a valve in combination with an installed flow meter (Bürkert Electro-Magnetic Inductive Flow measurements,



Fig. 2. Pulley system, from left to right: distance encoder, load cell, support pulley, stepper motor.



Fig. 3. Experimental Set-up.

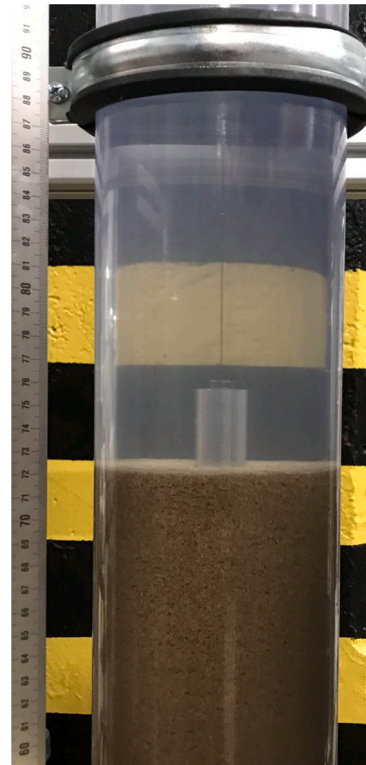


Fig. 4. Submerged object.

type 8051). Water temperature could be regulated with a boiler, a cooler, and a thermostat by recirculating water through a buffer vessel connected to a water reservoir. To measure the particle bed height, a metallic measuring tape was secured on the outer wall of the expansion column. A schematic overview can be found in Fig. 6. Additional technical information about materials is given in the supplementary material (Section 3).

2.2. Hydrometer pulley system

A pulley system driven by a stepper motor was mounted above the expansion column to move a cylindrical object vertically through the fluidised bed (Fig. 4). A distance encoder was used to measure the number of rotations (Fig. 2) which was converted to the longitudinal position of the object. A load cell measured the amount of strain in voltage which was converted to the weight of the object. The stepper motor, distance encoder, and load cell were connected to a I/O hardware module (Q.monixx) [21]. The module (Fig. 5) transmitted the data stream of and from Gantner GI.Bench data acquisition software environment running on a computer. Within the GI.Bench configuration [22], hardware controls and data log settings were defined, as well as the calibration values for conversion of strain [V] to mass [kg], and number of revolutions [#] to distance travelled [m]. The pulley system (Fig. 2) is composed of four components to move the object up and down the column and log its weight and distance. From left to right, the object is attached to a thin, braided fishing line. The line is strung over the first pulley, encoded with a step counter, which transmits the number of steps from a set zero point to an attached data processor. This relates to the area of the column in which the object resides. The line passes under the second pulley equipped with a load cell that measures the amount of strain in voltage. This strain is directly correlated to the submerged weight of the object which is calculated by calibrated values within the



Fig. 5. Data transfer unit.

GI.bench software. The line is threaded over the third pulley for support and connected to the stepper motor used to move the object up and down the column. Additional technical details are provided in the Supplementary material (Section 3).

2.3. Particle selection

The focus of this research is the development of a novel sensor for pellet-softening fluidised bed reactors. For this reason, polydisperse calcite pellets (100 % CaCO_3) were extracted from full-scale reactors. Relatively monodisperse fractions were obtained by sieving pellets batches with a AS 200 Retch Laboratory sieve shaker and calibrated US mesh sieves regulated by standards such as ISO 3310-1, ISO 565, EN 933-2 and ASTM E11 [23]. In addition, crushed calcite grains (100 % CaCO_3 from the Calcite Factory) were used to compose a two-fraction mixture. As a reference, spherical glass beads were used (Boom lab). Two representative samples from each fraction were scanned and analysed using ImageJ [24] to validate the particle size and morphological properties. The sieved fractions were used to compose three different particle beds for the fluidisation experiments. Additional morphological properties, such as the sphericity, were determined with a Retsch Camsizer XT [25]. Additional photos of examined granules are given in the Supplementary material (Section 2). Scanning Electron Microscope photos of calcite pellets were taken by Dirken et al. [26].

2.4. Fluidisation experiments

A straightforward pilot test was performed in a full-scale pellet-softening reactor to discover whether a submerged weight gradient was observed and measurable. Fluidisation measurements with glass beads were executed in a pilot set-up to analyse the influence of the dimensions of the submerged objects at maximum flow rate. Additionally, a series of

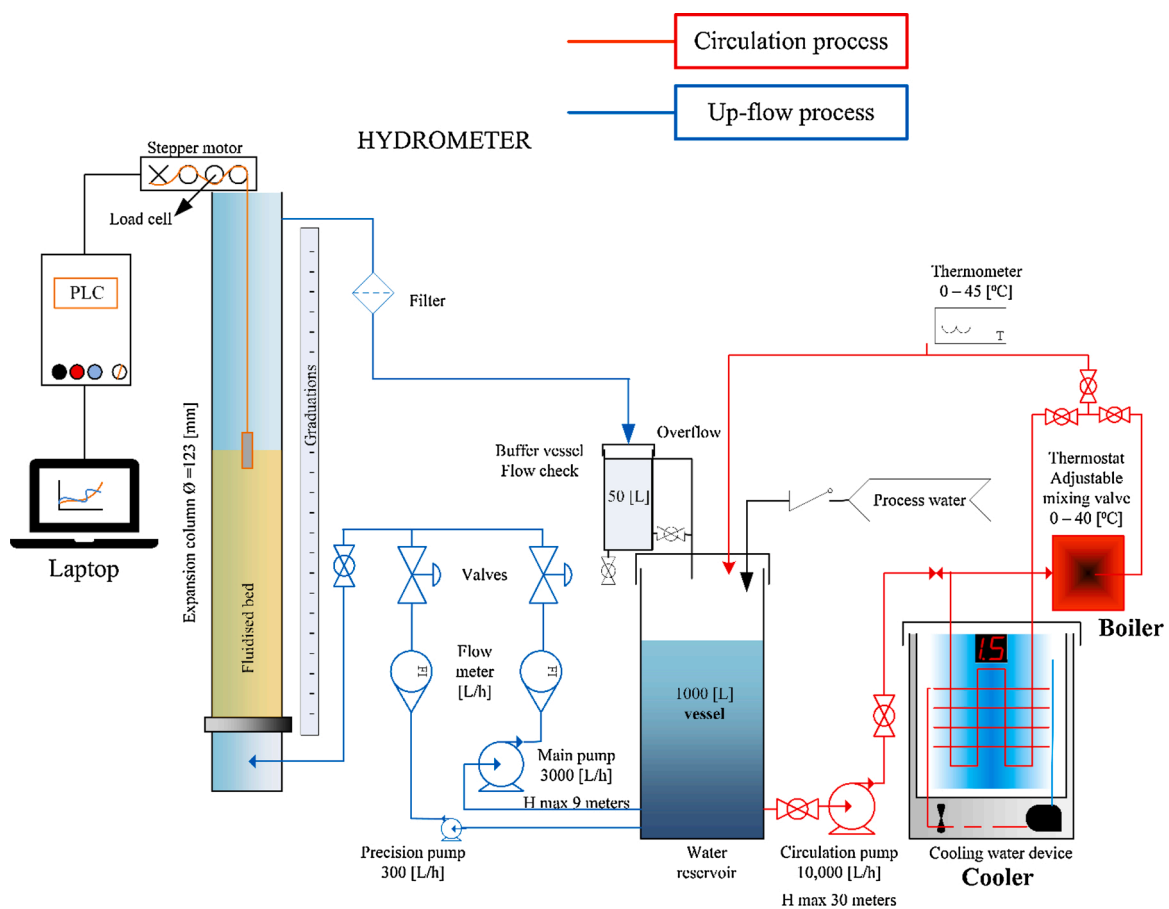


Fig. 6. Schematic representation of the experimental set-up. The system has two main circuits in which water flows: the expansion circuit and the temperature conditioning circuit. In the expansion circuit, a pump takes water from a reservoir and feeds it to the expansion column with an adjustable water flow. The flow rate entering the system can be controlled by opening and closing a valve and is measured by a calibrated flow meter. The temperature circuit consists of a pump that feeds water into an integrated heating or cooling unit equipped with a thermostat. Particles are fluidised in a cylindrical tube. The object weight and height is measured with the hydrometer soft sensor.

fluidisation experiments was performed with different calcite particles for various flow rates to measure longitudinal gradients. During these fluidisation experiments, the weight loss of the submerged object was measured while altering the height of the object. The fluid velocity and temperature were logged as well as the bed height.

2.5. Data transformation model

The buoyant weight gradient in the fluidised bed can be measured with the hydrometer sensor (Fig. 7). The measured strain is converted through a calibration curve into weight loss. The pseudo fluid or suspension density is calculated accordingly (explained in Section 3.1). The voidage can be derived based on a mass balance (Section 3.2). Since the initial particle mass and bed height were carefully measured, the particle mass, volume and total pressure drop are known (Section 3.4). Using this information, the estimated variables can be validated (Section 3.6). Using a data-driven model, the particles size can be estimated (Section 3.7). Combining the voidage and particle size, accordingly the reactor key performance indicators can be approximated (Section 3.8). Corrections for the influence of the submerged object on the voidage are proposed in Section 3.5.

3. Theoretical hydraulic state determination

3.1. Suspension density

Fluidisation is the process of converting a granular material from a static solid-like state to a dynamic liquid-like state of a suspended particulate assembly by introducing upward flowing fluid [27,28]. The apparent density of the particle-fluid mixture is larger than the fluid density itself. Assuming a homogeneous particle-fluid mixture in a fluidised bed [29], the average suspension density ρ_{mix} is directly related to the fluidised bed voidage ε [30]:

$$\varepsilon = \frac{(\rho_p - \rho_{mix})}{(\rho_p - \rho_f)} \quad (1)$$

Where ε is the voidage of the system, ρ_p the particle density and ρ_f the fluid density. Eq. (1) is valid under homogeneous fluidisation conditions. The average pressure drop ΔP over a vertical length z of the bed according to an elementary force balance states:

$$\Delta P = \rho_{mix} g z \quad (2)$$

In Eq. (2), fluid and solid wall friction from upward fluid flow is neglected when the column diameter is large. The pressure gradient (Eq.

(2)) is analogous to that in a Newtonian liquid, where the liquid density ρ_f is replaced by the suspension mixture ρ_{mix} . The suspension density gives rise to a buoyancy force F_b exerted on an object with volume V submerged in the suspension analogous to the Archimedean buoyancy for a static liquid [31]:

$$F_b = \rho_{mix} g V \quad (3)$$

Eq. (3) is valid if the submerged object size is considerably larger than the particle size.

3.2. Force balance

In the absence of a surrounding medium, a stationary object suspended on a wire experiences a net zero force ($F_g = F_s$), given by Eq. (3), where F_g is the downward gravitational force, and F_s a measurable upward strain force on the wire. In air these forces are almost equal; in a fluidised bed however, the considerable upward buoyancy force F_b causes a difference between the dry weight F_g and the apparent weight F_s . Another contribution to this weight loss, albeit less dominant, is the upward drag force F_d caused by the fluid flow. All together this leads to Eq. (4):

$$F_s = F_g - F_b - F_d - F_{col} \quad (4)$$

Where F_{col} is related to the surface integral of solid stress over the surface area of the object similar to F_d , the surface integral of fluid stress over surface area of the object. When there is a strong gradient in solid concentration over the object, a higher concentration at the object bottom will result in an upward net collision force *i.e.* F_{col} will depend on the concentration. The stress depends on the Stokes number. Concerning calcite pellets, $St = 0.2 \pm 0.05$ and therefore the collision forces [32] are ignored or $F_{col} = 0$. An extensive analysis can be found in the Supplementary material (Section 4). Including other forces such as lift, added mass and Basset history forces, leads to considerably more complex expressions [33] but these are all negligible and therefore not the focus of this research.

3.3. Suspension density

Eq. (4) can be transformed into Eq. (5) accordingly:

$$m_{strain} = m_g - V_{object} \rho_{mix} - \frac{1}{2} \rho_{mix} v_i^2 \frac{A_1}{g} C_w \quad (5)$$

This approach is valid when the Stokes number is sufficiently small, such that the particles follow the flow. Combining Eqs. (5) and (1) leads

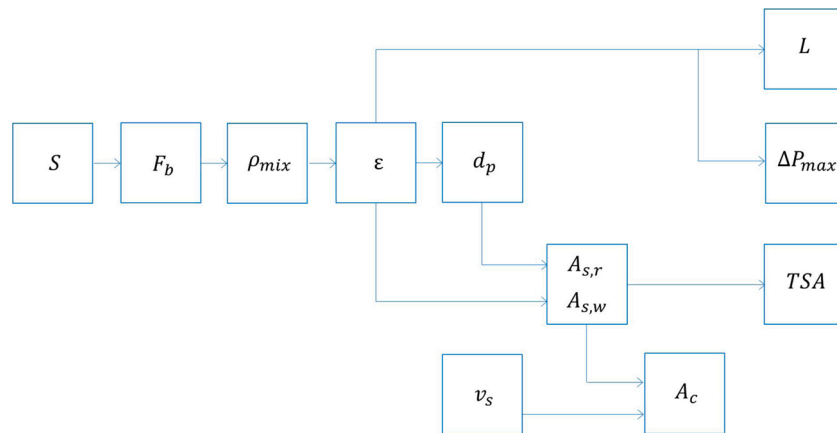


Fig. 7. Schematic representation of the data transformation model. Direct strain measurement is converted into weight loss, suspension density and accordingly voidage and estimated particle size. Specific surface area based on the reactor and water phase, reactor key performance indicators (Section 3.8) can subsequently be calculated.

to an explicit equation for the voidage, expressed as:

$$\varepsilon = \frac{\rho_p - \frac{m_g - m_{\text{grain}}}{V_{\text{Displaced}} + \frac{1}{2} \frac{A_{co}}{A_1} v_f^2 C_w}}{\rho_p - \rho_f} \quad (6)$$

Eq. (6) may be used on the assumption of a small Stokes number, where the apparent liquid mass density in the drag force is ρ_{mix} . The drag coefficient C_w in Eq. (6) is dependent on the particle-fluid suspension and flow velocity. To investigate the relevance of C_w and the hydrodynamic forces, the linear flow rate during the experiments was increased up to 64 mm/s. Even at the highest flow velocity, the hydrodynamic drag term ($\frac{1}{2} \rho_{\text{mix}} v_f^2 A_{co} C_w$) is rather small compared to the buoyancy term ($\rho_{\text{mix}} g V_{\text{object}}$), and could therefore be neglected (max 0.16 %), in particular regarding the operational window (17–25 mm/s) of full-scale pellet-softening reactors. Also, the influence of linear thermal expansion was examined and could be neglected as well (max 0.06 %). Derivations of given equations and tests in an empty column are provided in the Supplementary material (Section 4).

3.4. Total particle mass and differential pressure

The local voidage can be determined with Eq. (6). The overall average voidage of the whole system can be calculated using Eq. (7), based on the initial dry particle mass and total observed fluidised bed height:

$$\varepsilon = 1 - \frac{m}{\frac{\pi}{4} D^2 L \rho_p} \quad (7)$$

In this research, the differential hydraulic pressure over the bed height was not measured directly. However, based on the particle mass and density it is straightforward to calculate the maximum pressure drop indirectly for the fluidised state (Eq. (8)). These values can be validated with data from previous research [9]:

$$\Delta P = \frac{m g}{\frac{\pi}{4} D^2} \left(1 - \frac{\rho_f}{\rho_p} \right) \quad (8)$$

3.5. Submerged object corrections

3.5.1. Constriction model to compensate velocity and voidage perturbations

Because the cylindrical object is suspended in the hydrometer tube, the superficial fluid velocity will be larger (approximately 3 %–12 %) due to the decreased surface area (Figs. 8 and 9). This causes a locally increased voidage at the height of the object. Therefore, a correction is imperative to estimate the voidage for the lower velocity corresponding to the undistorted bed. Based on accurate expansion experiments [9] an empirical relationship (Voidage Power Function) between the voidage and the superficial fluid velocity was derived and used to determine a correction for the voidage.

From expansion experiments for a myriad of granules and expansion data provided from literature [34], a general fit parameter is found. Subsequently, Eq. (9) can be used to compensate the constriction effects caused by the cylindrical object submerged in the fluidised bed:

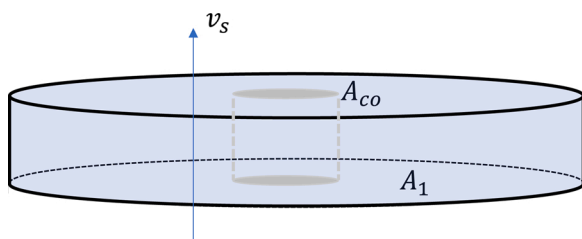


Fig. 8. Constriction model: schematic overview of a cylindrical object submerged in a fluidised bed.



Fig. 9. Largest cylindrical object.

$$\varepsilon_1 = \varepsilon_2 \left(1 - \left(\frac{D_{co}}{D_{hm}} \right)^2 \right)^{\frac{1}{3}} \quad (\varepsilon_1 < \varepsilon_2); (\varepsilon_{mf} < \varepsilon < 0.95) \quad (9)$$

Where ε_1 is the (corrected) voidage at situation 1 with no distorted bed, ε_2 (uncorrected) at situation 2 where the flow is restricted due to submerged object in the fluidised bed. D_{co} is the diameter of the cylindrical object and D_{hm} the inner column diameter of the hydrometer. The derivation of Eq. (9) is given in the Supplementary material (Section 4).

3.5.2. The influence of the object dimensions on the prediction accuracy

To investigate the influence of the object dimensions on the prediction accuracy, the fluidisation quality and the number of particles in the vicinity of the object was determined. The Froude number is defined as the ratio of inertial to gravity forces [35]. The densimetric particle Froude number Fr_p [36,37,34]; can be used as a proxy for the fluidisation quality from smooth homogeneous (particulate) fluidisation to heterogeneous or aggregative (bubbling) fluidisation, expressed in Eq. (10):

$$Fr_p = \frac{v_s}{\sqrt{\left(\frac{\rho_p}{\rho_f} - 1 \right) g d_p}} \quad (10)$$

A transition occurs from particulate or smooth homogeneous fluidisation to heterogeneous or aggregative (bubbling) fluidisation at $Fr_p = 1$ [38,28,29]; mostly for gas-solid systems, but lower values are also proposed: $Fr_p < 0.13$ [39]. In general, the transition from a homogeneous to a heterogeneous state is gradual.

The validity of the suspension mixture density ρ_{mix} depends on the number of rigid particles around the submerged object. The estimate of the number of particles in a layer around the submerged object is based on the assumption that the particles are spherical and equidistant. The average distance between the centres of two spherical particles Δd_p in fluidised state can be calculated with Eq. (11):

$$\Delta d_p = d_p \sqrt[3]{\frac{\pi}{(1 - \varepsilon) 3\sqrt{2}}} \quad (11)$$

If the layer around the object is ξ particles thick, the number of particles N_p around the submerged object can be calculated with Eq. (12):

$$N_p = \left(\frac{L_{co}}{\Delta d_p} + 2\xi - 1 \right) \left(\pi \left(\frac{D_{co}}{\Delta d_p} + 2\xi \right) - 1 \right) \quad (12)$$

Derivations can be found in the Supplementary material (Section 4).

3.6. Discretisation modelling

3.6.1. Bed height

The fluidised bed in the column can be subdivided into segments. By gradually lowering the submerged object, for every measurement, the position, weight loss and accordingly the voidage (Eq. (6)) can be determined. This way, the gradient in the particle bed can be obtained. In principle, two constraints apply to the segment heights and local voidage values: first, the sum of N segment heights should be equal to the total bed height L (Eq. (13)), and second, the total solid mass should be conserved (Eq. (14)):

$$L = \sum_{i=1}^N \delta z_i \quad (13)$$

$$\sum_{i=1}^N (1 - \varepsilon_i) \delta z_i = L_0 (1 - \varepsilon_0) \quad (14)$$

In practice, a deviation between the sum of $(1 - \varepsilon_i) \Delta z_i$ and the total measured value $L_0 (1 - \varepsilon_0)$ can be expected. Based on Eq. (14), it is possible to calculate a correction factor f (universally applied to the estimated voidages at all heights) that can be used to compensate for the deviation:

$$f = \frac{L - L_0 (1 - \varepsilon_0)}{\sum_{i=1}^N \delta z_i \varepsilon_i} \quad (15)$$

So, $\varepsilon_{i,corr} = f \varepsilon_i$ such that $\sum_{i=1}^N (1 - f \varepsilon_{i,corr}) \delta z_i = L_0 (1 - \varepsilon_0) = L (1 - \varepsilon)$ hence:

$$L = f \sum_{i=1}^N \delta z_i \varepsilon_i = L_0 (1 - \varepsilon_0) \quad (16)$$

3.6.2. Differential pressure

In a homogenous steady fluidised state, the hydraulic pressure drop equals the weight of the particle bed, reduced by the buoyancy forces, per unit of bed volume [38]. In the presence of a vertical gradient, the summed differential pressures per segment (Eq. (17)) must be equal to the total pressure drop according to Eq. (8):

$$\Delta P_{max} = g (\rho_p - \rho_f) \sum_{i=1}^N (1 - \varepsilon_i) \delta z_i \quad (17)$$

Where $\varepsilon_i = \varepsilon_{i,corr}$ from Eq. (16).

3.6.3. Number of particles in the system

Assuming spherical particles, Eq. (18) can be used to estimate the number of particles in one particular segment in the fluidised bed in a cylindrical column:

$$N_i = \frac{3}{2} (1 - \varepsilon_i) \frac{D^2}{d_p^3} \delta z_i \quad (18)$$

Accordingly, the total solid particle area in the bed volume is the sum of all the particle surfaces combined: $\sum N_i A_{1p}$ leading to the total surface area TSA in the entire fluidised bed:

$$TSA = \frac{3}{2} \pi D^2 \sum_{i=1}^N \frac{(1 - \varepsilon_i)}{d_{p,i}} \delta z_i \quad (19)$$

3.7. Particle size estimation

Accurate expansion experiments [9] combined with symbolic regression techniques [40] have provided an empirical data-driven model to predict the voidage as a function of the fluid and particle properties. This same approach was applied to predict the (spherical) particle size conversely as a function of the superficial fluid velocity, kinematic viscosity, particle density and measured voidage following Eq. (20):

$$d_p = v_s^{c_0} \nu_T^{c_1} \left(\frac{\rho_p}{\rho_f} - 1 \right)^{c_2} (c_3 \varepsilon^{c_4} + c_5 \varepsilon^{c_6}) \quad (\varepsilon_{mf} < \varepsilon < 0.95) \quad (20)$$

Fitting parameters for calcite pellets, glass beads and highly spherical particles were obtained using non-linear regression software and are given in Table 1. Model explanation, sources, and further fitting parameters for other types of granules are given in the Supplementary material (Section 4).

3.8. Model-based hydraulic state determination and reactor performance indicators

If the voidage and the (spherical) particle diameter are known, reactor Key Performance Indicators (KPIs) can be calculated [9]. The most commonly applied KPI is the specific surface area (SSA) which represents the available area per m^3 reactor volume for crystallisation [3,1,28]. The reactor performance indicators used are the specific surface area based on the reactor volume $A_{s,r}$ and the specific surface area based on the water phase $A_{s,w}$:

$$A_{s,r} = 6 \frac{1 - \varepsilon}{d_p} \quad (21)$$

$$A_{s,w} = \frac{A_{s,r}}{\varepsilon} \quad (22)$$

In addition, the specific space velocity A_c is used [9] defined as the contact area per second per m^2 of transfer surface area [41]. The specific space velocity (SSV) is defined as:

$$A_c = A_{s,w} \frac{v_s}{\varepsilon} \quad (23)$$

Please note that A_c is an inverse time scale with units $[s^{-1}]$, while their counterparts $A_{s,r}$ and $A_{s,w}$ are both inverse length scales with units $[m^{-1}]$.

Discretised KPIs can be found in the Supplementary material (Section 6).

4. Results and discussion

4.1. Preliminary full-scale experiment

To explore the possibility of measuring a weight gradient in a liquid-solid fluidised bed, an object was submerged in a full-scale pellet-softening reactor (Fig. 11) with a diameter of $D = 2.6$ m and a bed height of $L = 4.20$ m. The superficial fluid velocity was $v_s = 24$ mm/s with a water temperature of $T = 12$ °C. A steel object was gradually submerged in the fluidised bed using a regular suspended scale. Additionally, 16 samples of calcite pellets were withdrawn at different heights. The grains were dried, sieved and analysed with image analysis software ImageJ [24]. The largest pellets were found at the bottom of the reactor ($d_p = 1.17$ mm) and the smallest at the top of the fluidised bed ($d_p = 0.47$ mm). The mass of the spherocylindrical object in air was 2.71 kg and submerged in water 2.45 kg. In Fig. 10, the decreasing object mass is plotted in black

Table 1
Fitting parameters in Eq. (20).

Grain material	Value	c_0	c_1	c_2	c_3	c_4	c_5	c_6	Correlation coefficient R^2
Glass beads		1.148	0.3060	-1.190	1.120	-3.050	5.875	1.475	0.990
Calcite pellets (calibrated data-set)		1.068	0.3101	-3.217	2.360	-3.069	11.73	1.059	0.968
Calcite pellets (validated data-set)		1.031	0.4264	-0.283	2.529	-3.161	6.938	0.808	0.915
Crushed calcite		0.613	0.4053	1.037	0.4764	-2.272	3,317	13.74	0.733

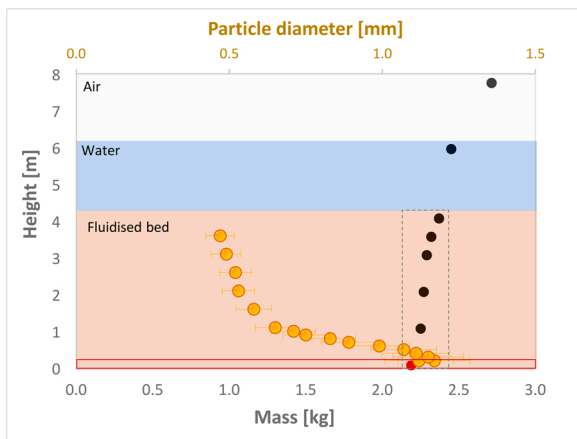


Fig. 10. Object weight measured (middle object) in softening reactor at various heights in air, water, and fluidised bed. Superficial fluid velocity 24 mm/s, water temperature 12 °C, bed height 4.20 m, maximum pressure drop 16.5 kPa. Steel spherocylindrical object 90 × 57 mm, volume 0.26 L, 2.71 kg in air, 2.45 kg submerged in water. The gradient difference in the fluidised bed $\Delta m/\Delta L \approx 0.045$ kg/m. Dotted grey frame indicates the measured gradient, ● the spherocylindrical submerged object, ● object near the reactor bottom, ● indicate the particle ImageJ/sieve diameter with error bars caused by the particle size distribution. Red frame indicates unstable zone caused by distributor ($z = 10$ cm).



Fig. 11. Full-scale pellet softening reactor top view, reactor diameter ($D = 2.6$ m).

circles against the position in the fluidised bed *i.e.* height. The mass gradually decreased from 2.37 kg in the top to 2.19 kg in the vicinity of the reactor bottom. The mass difference (decreased mixture mass density and hence the variation in particle volume concentration) in the fluidised bed was 0.18 kg corresponding to 0.7 mm difference in particle size. Based on this indicative result, a new pilot plant set-up was designed in which 40 experiments were prepared and executed, which are discussed in the next Section.

4.2. Particle selection

For the fluidisation experiments, 5 kg of glass beads were purchased, and a total of 30 kg of calcite pellets was fractionated (Table 2) to obtain the best achievable monodisperse particles. The particle density was measured through a laboratory pycnometer with an error of 0.5 %. The particles sizes were measured using a classical sieve analysis, image analysis and additionally with a Camsizer for validation purposes. Compared to the sieve mesh size, the particle size of the relatively spherical calcite pellets (sphericity $\phi_s \approx 0.95$) was approximately 5 % larger when determined with the Camsizer, and approximately 13 % larger when determined with ImageJ. For the irregularly shaped, crushed calcite (sphericity $\phi_s \approx 0.90$), the differences were 14 % and 36 % for the Camsizer and ImageJ, respectively. These differences were presumably caused by the particle orientation. Particles pass through a sieve mesh vertically oriented, whereas scanned particles orient horizontally during the ImageJ analysis [42]. Photographs, particle properties and technical details of used equipment are provided in the Supplementary material (Sections 2 and 3).

4.3. Proof of concept of the hydrostatic weighing technique

Initially, 9 fluidisation experiments were executed with glass beads at high velocity, to investigate the influence of the size of submerged objects on the accuracy of voidage determination. For this research, a total of 40 fluidisation experiments were conducted with calcite pellets and crushed calcite. To demonstrate the weight gradient over the bed height, 9 fluidisation experiments were executed with a mixture of calcite and crushed calcite fractions (Table 2). Accordingly, to study the prediction accuracy of the voidage and (spherical) particle size, two relatively monodisperse particles samples of calcite pellets were used. Finally, 4 additional experiments were performed with an alternative submerged object material.

4.3.1. Submerged object dimensions

Experiments were executed in the experimental set-up with monodisperse glass beads (Fig. 12) to scrutinise the dimensions of the submerged objects and to validate the constriction model (Eq. (9)). A total of 9 aluminium cylinders (Fig. 13) with varying dimensions were compared at a high superficial fluid velocity ($v_s = 67$ mm/s).

The reason for choosing aluminium objects was based on an expected voidage in the lowest region of the pellet-softening reactor. A usual voidage $\varepsilon \approx 0.55$ leads to a suspension density of 1,750 kg/m³ (Eq. (1)). To prevent floating, the density of the submerged object must be larger than the suspension density. It has, however, to be small enough to maintain an object mass within the measurement range, and to have a large enough object size to be in the correct limit of being much larger than the particle size.

Table 2
Particle properties of examined granules used in the hydrometer measurements.

Fraction [#]	Grain type	Geldarts particle type ¹	Particle size min-max [mm] ²	Dry weighted particle mass [kg]	Particle density [kg/m ³]	Sieve diameter [mm]	Camsizer diameter [mm]	ImageJ diameter [mm]	Sphericity [-]
Particle bed 0	Glass beads	D	3.03–3.14	4.95	2,515	–	–	–	0.99 ³
Particle bed 1	Calcite pellets	B	0.80–0.90	10.00	2,614	0.95	0.99	1.06	0.94
Particle bed 2	Calcite pellets	D	0.90–1.00	10.00	2,625	0.56	0.64	0.76	0.95
Particle bed 3: (two fractions)	Calcite pellets + Crushed calcite	B D	0.50–0.63 1.25–1.40	4.00 6.00	2,560 2,632	1.32 0.85	1.37 0.90	1.50 0.97	0.90 0.97

¹ Geldarts particle classification [43]. Type B; sand-like particles and type D: spoutable particles.

² The effective or average hydraulic equivalent particle diameter $d_p = \sqrt{d_{s,1} d_{s,2}}$, [1,44].

³ Sphericity of glass beads is obtained from literature [45,46,34]. Sphericity is the ratio of the surface area of an equal volume sphere to the surface area of the grain calculated from the perimeter P and project area.



Fig. 12. 3 mm glass beads (Boom lab) at $v_s = 67$ mm/s.

Based on the measured ‘submerged object voidage’ (Eq. (6)) and the average voidage of the whole system (Eq. (7)), the average relative prediction error (Eq. (24)) was calculated, indicated with blue circles in Fig. 15, using Eqs. (6) and (7):

Fig. 13. Aluminium cylindrical objects, ($L_{co} = 100, 120, 160$ mm • $D_{co} = 20, 30, 40$ mm), $\rho_p = 2,701$ kg/m³.

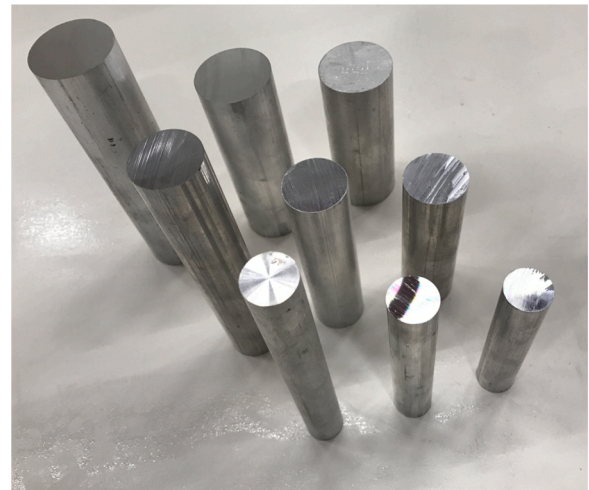


Fig. 14. Titanium cylindrical object, ($L_{co} = 130$, • $D_{co} = 35$ mm), $\rho_p = 4,464$ kg/m³.

$$ARE = \frac{1}{N} \sum_{i=1}^N \left(\frac{|\epsilon_{calc,i} - \epsilon_{exp,i}|}{\epsilon_{exp,i}} \right) \quad (24)$$

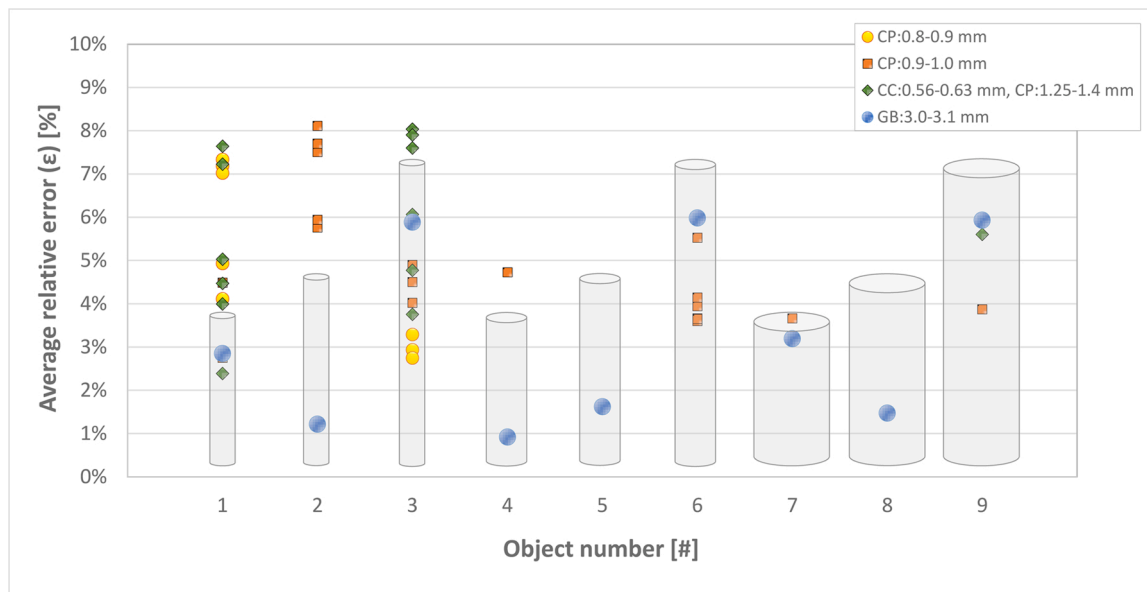


Fig. 15. Average relative error (Table 3) estimated voidage against the cylindrical object number (Fig. 13). Yellow circles: calcite pellets (0.80–0.90 mm), orange squares: calcite pellets (0.90–1.00 mm), green rhombus: mixture of crushed calcite (0.50–0.63 mm), calcite pellets (1.25–1.40 mm) and blue circles: glass beads (3 mm). The constriction model (Eq. (9)) was used to compensate fluid velocity and voidage changes caused by the object in the cylindrical column.

The average relative error for the six aluminium objects ($L_{co} = 100$ and 120 mm) was 2 %. For the three aluminium objects ($L_{co} = 160$ mm), the relative error was 6 %. The objects were submerged approximately 10 cm in a fluidised bed of glass beads with an expanded bed height of 41 cm. The longest objects, only 14 cm in the vicinity of the fluid distributor, showed a larger error compared to the objects with a shorter length. This was probably caused by the heterogeneous flow distribution in the bottom of the column. The lowest error of 1 % was found for the cylindrical objects with the largest width, presumably due to its higher mass, causing it to be more stable in the fluidised bed. In addition, elongated cylinders tend to rotate to maximise their cross-sectional area A_{\perp} of the object perpendicular to the flow. In addition, the error was calculated for all other fluidisation experiments and is presented in Fig. 15. The overall average relative error was 5 ± 2 %. The results are not conclusive regarding the choice of the most optimal object dimensions. There are certainly more effects governing the voidage prediction accuracy, such as object density, shape, and (semi) homogenous fluidisation. The effect of object dimensions however seems to have been compensated for by using the constriction model, as shown in Eq. (9). The effect of constriction was visible during the measurements. Upon lowering the object, a decreased weight was observed for a period of 5–10 seconds. Presumably, during this period, the fluidised bed voidage re-adjusted to the altered flow caused by the presence of the object. After this effect subsided, the average weight remained constant, however fluctuations were still present, especially in the lower regions of the column. This was most likely caused by an inhomogeneous particle bed in the vicinity of the water distributor at the bottom of the column resulting in object swaying. The maximum fluctuation was ± 2 g and is considered in the Data transformation model error analysis in Section 5 of the Supplementary material.

To investigate the influence of the object density, four additional experiments were performed with a titanium cylindrical object ($L_{co} = 130$, $D_{co} = 35$ mm) shown in Fig. 14. The average prediction error for the voidage was 4 ± 2 % but the observed instabilities in the lower region of the cylindrical column ($z < 10$ cm) did not decrease. Therefore, in this research we could not explicitly determine the optimal material density for the submerged object for the use in a pellet-softening reactor.

The densimetric particle Froude number Fr_p was calculated (Eq. (10)) to obtain information about the prevailing fluidisation quality. Predictions errors against the Froude number does not indicate that

heterogeneous unsteady behaviour [47] is a determining factor. Figures can be found in the Supplementary material (Section 4).

Eq. (12) was used to estimate the number of particles in a layer around the submerged object to examine if the suspension density assumption is not violated. When the layer around the object is ξ is set to 1, the minimum number of particles around the submerged object was approximately 1,000 (maximum 25,000), sufficient to apply the hydrostatic weighing technique to estimate the voidage. Although no adverse influence was found related to the number of surrounding particles, it is not clear below which number the accuracy will decrease. The glass beads measurements appear to be more accurate compared to pellets, but please note that the data spread for all grains examined is more or less the same at 5 %. In addition, figures with predictions errors can be found in the Supplementary material (Section 4).

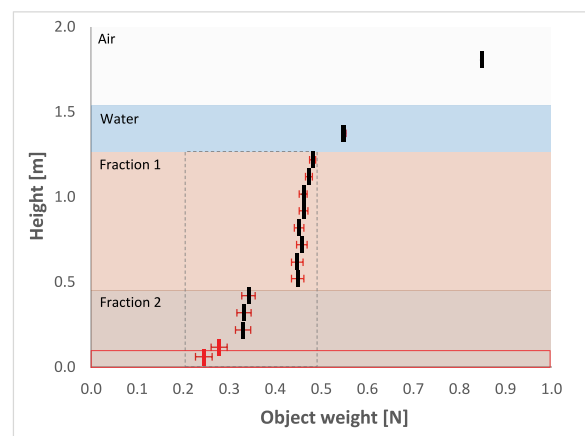


Fig. 16. Experiment #31. Object weight was measured (middle object) at various heights in air, water, and fluidised bed fractions. Superficial fluid velocity 28 mm/s. Water temperature of 11 °C. Aluminium cylindrical object 100.09 × 20.05 mm, volume 0.032 L, 0.85 N in air, 0.55 N submerged in water. Error bars indicate observed fluctuations during measurements. Dotted grey frame indicates the measured gradient. Red frame shows unstable zone caused by distributor instabilities ($\Delta z = 10$ cm). Measurements in this zone are excluded and marked red.

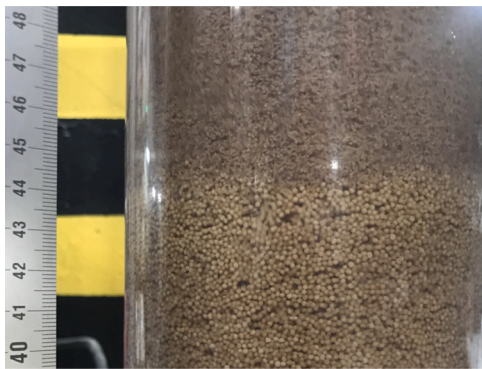


Fig. 17. Two fractions mixture: crushed calcite grains 0.50-0.63 mm at the top and calcite pellets 1.25–1.40 mm at the bottom.

4.3.2. Expansion experiments for the gradient determination with a two fractions mixture

Fluidisation experiments were performed in four differently sized calcite fractions as shown in Table 2. The goal of the first experiment was to show that a sharp gradient in the longitudinal direction can be measured. To this end, a mixture of grains was composed of two fractions (Fig. 17). The grains represent the extremes in particle size and position in a full-scale pellet-softening reactor: the largest calcite pellets 1.25–1.40 mm can be found in the lowest region of the reactor while crushed calcite grains 0.50-0.63 mm can be found in the top of the fluidised bed. In a series of experiments ($N = 13$) with the double fraction calcite mixture, the object was gradually lowered in the fluidised bed shown in Table 3. The weight gradient can be identified in Fig. 16 ($0.3 < W_{sub} < 0.5$ N). During the experiments, instabilities were observed in the lower region of the cylindrical column (< 10 cm). These values were omitted from the results (indicated in red). Supporting arguments for removing these data points are that in later optimising studies, instabilities can be prevented or resolved by better object design. All experimental data has been shared in the Supplementary material (Section 9).

The density gradient (Eq. (6)) is clearly visible in Fig. 18. The green rhombuses represent the middle of the object where the gradient among the object length was averaged. The voidage, based on the Archimedes' principle (Eq. (6)) was compared with the bed height (Eq. 14) and mass-based mean voidage (Eq. (7)). In this way, the gradient could be validated. Fig. 19 shows that there is an increasing deviation between the local voidage and the mean system voidage when lower regions are reached. This deviation was a generally consistent trend for the majority of the experiments. The observed slope in Fig. 19 for the local voidage is caused by a prevalent stratification of grains in the range 0.50 to 0.63 mm where the 'largest' grains can be found in the lowest zone of this fraction and vice versa. The explanation for the absolute deviation can be explained by calibration inaccuracies, hysteresis and a non-optimal object density. Although the load cell was carefully calibrated to

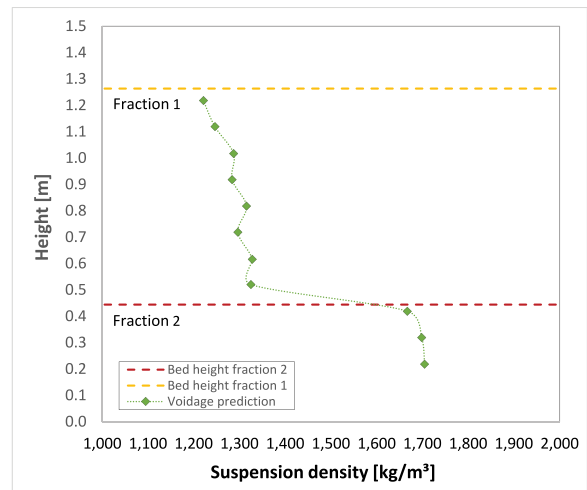


Fig. 18. Suspension density ρ_{mix} derived from weight measurements at various heights. Individual fractions are presented by yellow and dark red dotted lines. The gradient difference in the fluidised bed $\Delta\rho_{mix} \approx 500$ (kg/m³)/m.

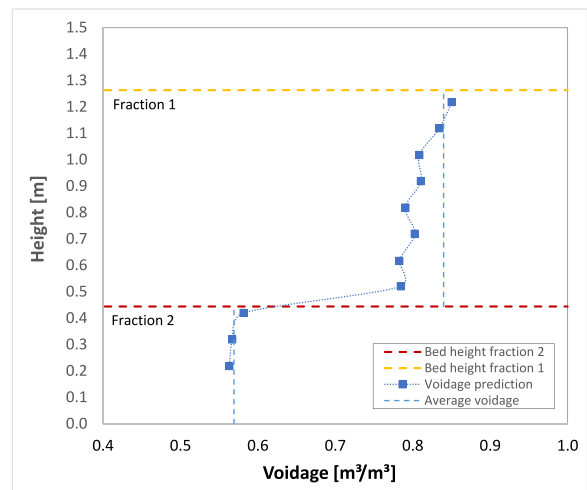


Fig. 19. Voidage ϵ derived from weight measurements at various heights. Blue dotted lines show the average voidage in respective fractions calculated independently, based on initial particle mass, particle density and bed height. The gradient difference in the fluidised bed $\Delta\epsilon \approx 0.3$ 1/m.

improve the strain measurement, errors were found between 0.5–1 %. Every deviation in strain corresponds with a comparable degree of error in voidage prediction error. Information about hardware calibration is provided in the Supplementary material (Section 3). Fig. 19 shows a zig-zag pattern which was the result of ascending and descending the object

Table 3
Aluminium object measures and voidage prediction error.

Object number [#]	<i>D</i>	<i>L</i>	<i>A</i>	<i>m</i>	<i>m_{sub}</i>	<i>ARE</i> (ϵ) GB:3.0 mm	<i>ARE</i> (ϵ) CP:0.8-0.9 mm	<i>ARE</i> (ϵ) CP:0.9-1.0 mm	<i>ARE</i> (ϵ) CC:0.50-0.63 mm CP:1.25–1.40 mm
	[mm]	[mm]	[mm ²]	[g]	[g]	[%]	[%]	[%]	[%]
1	20.05	100.09	316	88.03	56.22	2.8	6.1	3.6	5.1
2	20.08	120.06	317	104.86	66.76	1.2	–	7.0	–
3	20.17	160.00	320	141.29	89.90	5.9	3.0	4.5	6.4
4	29.92	100.38	703	202.16	131.50	0.9	–	4.7	–
5	29.92	120.13	703	230.70	146.42	1.6	–	–	–
6	29.92	160.00	703	320.72	208.34	6.0	–	4.1	–
7	40.06	100.52	1,260	342.76	216.68	3.2	–	3.7	–
8	40.00	120.09	1,257	408.52	258.18	1.5	–	–	–
9	40.01	160.00	1,257	545.26	344.32	5.9	–	3.9	5.6

within the fluidised bed but also due to hysteresis. The hardware shows a minor sensitivity of 3 % of the total range (2 kg) for hysteresis. In addition, due to the shape of the cylindrical object, a few grains tend to settle on the top of the surface of the object. Approximately for every gram of *hitchhiking* grains, the voidage prediction error increases with 1 %. In this research, aluminium cylindrical objects were used to match the expected fluid suspension density. The effect of adjusting the object density has not thoroughly been investigated in this research. Despite the observed deviation, this experiment with two fractions clearly demonstrated the potential to measure a gradient, and estimate the voidage at any height except the lowest 10 cm.

Please not that in Figs. 19 and 20 the voidage was not corrected with Eq. (16). Using a correction, the voidage prediction would be centred around the average voidage such that the average over the voidage prediction within a layer matches with the average voidage of that layer.

4.3.3. Single fraction experiments

Next, two single fractions of calcite pellets were used to examine whether the spherical particle size can be predictive using a data-driven model (Eq. (21)) based on the known particle fluid properties. Fig. 20 demonstrates the existence of a gradient for both voidage and estimated (spherical) particle size (Eq. (21)). The stratified bed and known sieve diameters enable the application of a linear interpolation of particle size over the length scale of the bed that better reflects the real situation. The voidage prediction results for all examined granules are presented in Table 3. The uncertainties regarding particle size comparison due to the different available image analysis methods are indicated with error bars (yellow).

As the fixed and fluidised bed heights were measured during the experiments, the mass balance could be used to validate the total bed height (Eqs. (13) and (14)). In addition, the summed differential pressures per layer (Eq. (18)) were used to compare with the total expected pressure drop (Eq. (8)). The prediction error for ΔP_{max} was approximately 7 % with a standard deviation of 5 % shown in Table 4. The extent of the error for bed height and differential pressure is strongly dependent on the quality of the voidage prediction. When the correction factor expressed in Eq. (15), was used, the overall voidage production accuracy was enhanced from 5 % to 3 %. This correction factor could be a solution in full-scale operations to cross validate measured and estimated process variables.

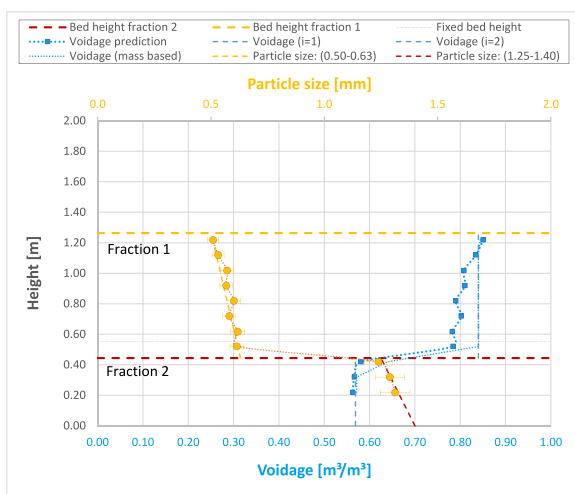


Fig. 20. Experiment #31. Voidage and particle size prediction at various heights. Individual fractions are presented by yellow and dark red dotted lines. Blue dotted lines show the average voidage in respective fractions calculated based on initial particle mass, particle density and bed height. Yellow circles show the average particle size in respective fractions calculated based on the empirical prediction model according to Eq. (20). The gradient difference in the fluidised bed $\Delta\epsilon/\Delta L \approx 0.3 \text{ m}^{-1}$ and $\Delta d_p/\Delta L \approx 0.8 \text{ mm/m}$.

Table 4 shows the particle size prediction errors using the novel data-driven model (Eq. (21)) and in addition, the prediction errors of the Carman–Kozeny and Ricardson–Zaki model. We prefer the data-driven model, fitted for non-spherical calcite pellets, not only for its slightly lower prediction error but mainly for the explicit expression for particle diameter. The particle size prediction quality depends largely on the accuracy of the voidage ($d_p \approx \epsilon^{-3}$). The dependency of the particle size on the voidage and figures with predictions errors can be found in the Supplementary material (Section 4). In addition, approximately 10 % uncertainty can be expected due to calcite pellets being fractionated with sieves with the minimum difference between two successive sieve meshes ($d_{s,1}/d_{s,2} = 10^{1/20} = 1.12$). Consequently, particle size estimation is only functional when the voidage determination is reasonably accurate. In addition, calcite grains are not completely spherical (Table 2) which implies a discrepancy between estimated and real particle size (and shape). In addition, bias is also expected from sieve analysis when particles are highly non-spherical such as crushed calcite.

4.3.4. Data-transformation-model

A sensibility analysis was conducted to determine the implications for the data conversion steps *i.e.* the data-transformation-model (DTM) presented in Fig. 7. The load cell measured the weight of the object expressed in voltage (error ≈ 0.6 %). Through a calibrated relationship, the buoyant forces and weight loss were determined with the software (error ≈ 3 %). Through a model (Eq. (1)), the suspension density was calculated (error ≈ 3 %). Accordingly, the voidage could be approximated with Eq. (6) (error ≈ 5 %). The particle volume, bed height and pressure drop based on the overall mass balance were used to optionally further validate these results (error: 7 %). Based on the voidage, the spherical particle diameter could be estimated with Eq. (21) but with a significant error ≈ 10 %. Using the summarised propagated effect of errors [49] an error of 7 % for ϵ , 12 % for d_p , and 14 % for SSA was calculated. A detailed table of the data-transformation-model with the expected influence on the voidage prediction dependency can be found in the Supplementary material (Section 5). The hydraulic state determination error arises from a quantitative starting point to be considered. Nevertheless, in full-scale operation 10 % uncertainty is acceptable for process monitoring and control, especially in view of the fact that currently there is no sensor available at such large scales.

5. Conclusions

A novel sensor has been developed, exploring the possibility of reasonably quick measurement of the hydraulic gradient in a liquid-solid fluidised bed applied in full-scale drinking water treatment plants. The preliminary test in a full-scale pellet-softening reactor at normal conditions was successfully performed to examine the existence of a gradient in the stratified bed. A mass loss of 10 % was measured over the reactor bed, corresponding to 0.7 mm difference in particle size. Hence, a lab-scale sensor was developed to measure the weight loss of a cylindrical submerged object while gradually lowering it in the particle bed. During fluidisation experiments of a two-layer calcite grains system, a steep gradient between different layers could be measured, starting from 0.85 N in air, 0.55 N submerged in water, 0.48 N at the top and 0.24 N at the bottom of the column. A weight loss of 50 % was measured over the fluidised bed, corresponding to 0.9 mm difference in particle size. Based on fluidisation experiments with two single layers of calcite pellets, the particle size was estimated with a new data-driven model. Voidage could be estimated with an error of 5 % and the spherical particle size with an error of approximately 10 %. A developed constriction model was suitable to compensate changes in fluid and voidage caused by objects suspended in the fluidised bed with different lengths and widths. The voidage prediction error could not be significantly be decreased by choosing other submerged object dimensions, nor did the prediction accuracy improve when aluminium was replaced by titanium. As a consequence, measurements in the lowest region of the

Table 4

Voidage, particle size and pressure drop prediction error. The last two columns are prediction errors after application of the voidage correction f (Eq. (15)).

Object number [#]	$ARE(\varepsilon)$ [%]	$ARE(d_p)^1$ [%]	$ARE\sum_{i=1}^{i=N}(1-\varepsilon_i)\delta z_i^2$ [%]	$ARE(\Delta P_{max})$ [%]	f [-]	$ARE(\varepsilon)$ [%]	$ARE(d_p)$ [%]
GB:3 mm	4.7	8.8	9.5	9.5	1.06	2.9	11.8
CP:0.80-0.90 mm	5.0	11.2	7.1	7.1	1.04	3.9	15.6
CP:0.90-1.00 mm	5.7	7.9	10.8	7.9	1.05	3.2	9.1
CC:0.50-0.63 mm CP:1.25-1.40 mm	3.2	5.3	3.1	3.1	1.03	0.8	3.6
Total average	4.8	8.8	7.8	7.0	1.03	3.0	11.0
Standard deviation	1.9	3.8	5.1	4.7	0.03	1.3	5.7

¹ Carman [15] results for comparison, respectively: 11 %, 9 %, 10 %, 5 % and for Richardson-Zaki [48] 21 %, 17 %, 18 % and 13 %.

² Eqs. (14) and (16).

column were omitted, which are probably influenced by instabilities in the vicinity of the fluid distributor plate.

The new sensor was tested as a proof of concept. Despite a 5 % prediction error for voidage, a 10 % error for the spherical particle size and an overall propagated error of approximately 20 % for the reactor key performance indicators, it was possible to measure a clear gradient in the liquid-solid fluidised bed during the experiments and in a full-scale reactor. This is promising for daily process control in full-scale reactors. The benefits of a longitudinal sensor for daily process control are quick access to the particle bed behaviour and, as a result, greater flexibility with changing water flow and process conditions. Impending problems such as fixed bed risk, flushing, hampering, or malfunctioning sensors such as differential pressure or bed height sensors can therefore be avoided. A potential downside compared to traditional differential pressure measurements is that the series of local measurements cost more time to process depending on the number of measurements performed. This could cause a delay for operational response to impending system changes. For the experimental setup, 20 local measurements could be achieved in ± 30 min.

If in future research the inaccuracies can be improved, reactor key performance indicators can be calculated in real-time to assess the hydraulic reactor performance and to support optimal states.

6. Recommendations

To improve the accuracy and reliability of this novel sensor, several aspects must be improved.

- The decreasing accuracy in the lowest region of the reactor. This is relevant since the highest chemical driving force occurs in that particular zone. Solutions can be found in the design of the submerged object, by optimising object dimensions, shape and density or using smart data filtering and processing.
- Combining the Archimedes-based hydrostatic weighing technique with an additional (submerged) differential pressure measurement device will make the discretised model validation more accurate.
- Adding a series of differential pressure meters over the height of the experimental fluidisation column will make validation of the results more accurate, along with making it possible to validate the gradient directly.
- The weight loss measurements with the new experimental set-up were executed and logged manually. Programming a routine (Q.monixx) can improve the data quality and decrease manual labour significantly.
- Substantiating a standard number of measurements sufficient for determining potential operational change, along with automation of the measurement could drastically decrease the time required for a profile measurement thereby minimizing the delay for operational response.
- During the measurements, the centre of the object was used as a reference point for the middle of a layer, in which the voidage was averaged. By subdividing the column into more segments through

introducing a gradual matrix data, more accurate voidage, particle size, and surface area gradients can be determined.

- In full-scale pellet-softening reactors at the Waternet facility Weesperkarspel, a biomass growth process was detected on calcite pellets, caused by bacterial colonisation captured in calcite structures [50] forming porous calcium carbonate coatings. Grains with biomass growth have capricious shapes with different expansion behaviour and accumulation in the fluidised bed causes a significantly higher degree of expansion. The sensor can be used to detect deviations in the preferred gradient.
- A sophisticated analysis regarding particle collisions with the Stokes number is useful for improving the voidage and particle diameter prediction accuracy.
- The scope of the novel sensor can be widened, through performing fluidisation experiments with other types of granules, such as rapid filter sand, granular activated carbon and anthracite grains.
- Additional research is required to determine the effect of density on object swaying and weight fluctuation to substantiate choice of object material before implementation. - Computational Fluid Dynamics simulations can help improving the particle-fluid-object interactions by including advanced detailed forces and hydraulic and hydrodynamic phenomena.
- The soft sensor could be used to derive more information from the fluidised bed by incorporating, for example, a turbidity meter, pH meter, or thermometer.

With further research, the hydraulic state should be combined with a chemical key performance indicator such as the calcium carbonate crystallisation potential (CCCP) [13,8]. This will lead to further opportunities to reduce the chemical demand in pellet softening reactors and to significant improvement in water treatment processes such as more flexible operations, better water quality, reduced risks for approaching undesirable fluidisation states, less chemical usage, and more sustainability.

Recommendations and potential benefits of the novel sensor in more detail can be found in the Supplementary material (Section 9).

Funding

This research project did not receive any specific grant from funding agencies in the public, commercial or not-for-profit sectors.

Declaration of Competing Interest

This research is part of the project "Hydraulic modelling of liquid-solid fluidisation in drinking water treatment processes" carried out by Waternet (the water utility of Amsterdam and surroundings), Delft University of Technology and HU University of Applied Sciences Utrecht. Financial support came from Waternet's Drinking Water Production Department.

Acknowledgements

We acknowledge and thank our students from Delft University of Technology, HU University of Applied Sciences Utrecht and Queen Mary University of London and in particular Gerard van Hassel, Victor Shao, Aisha Malik and Roy Duijnmaijer for the precise execution of many laboratory and pilot plant experiments.

For our simulation, we used data acquisition software GI.bench. We thank Gantner for allowing us to use their software.

Appendix A. Supplementary data

Supplementary material related to this article can be found, in the online version, at <https://doi.org/10.1016/j.jwpe.2021.102091>.

References

- [1] J.C. Crittenden, R.R. Trussell, D.W. Hand, K.J. Howe, G. Tchobanoglous, *MWH's Water Treatment: Principles and Design*, 3rd ed., John Wiley & Sons, New York, 2012.
- [2] A.J. Graveland, J.C. van Dijk, P.J. de Moel, J.H.C.M. Oomen, *Developments in water softening by means of pellet reactors*, *J. AWWA Am. Water Works Assoc.* 75 (1983) 619–625.
- [3] J.K. Edzwald, *Water Quality and Treatment: A Handbook on Drinking Water*, 6th ed., American Water Works Association, American Society of Civil Engineers, McGraw-Hill, New York, 2011.
- [4] M. Beeftink, B. Hofs, O.J.I. Kramer, I. Odegard, A. Wal van der, Carbon footprint of drinking water softening as determined by life cycle assessment, *J. Clean. Prod.* 278 (2021) 1–10, <https://doi.org/10.1016/j.jclepro.2020.123925>.
- [5] J.A.M.H. Hofman, O.J.I. Kramer, J.P. van der Hoek, M.M. Nederlof, M. Groenendijk, Twenty years of experience with central softening in the Netherlands, water quality, environmental benefits and costs, in: *Water 21, International Symposium on Health Aspects of Calcium and Magnesium in Drinking Water*, MD. International Life Sciences Institute, 24–26 April 2006, Washington, DC., USA, 2007, pp. 1–8. <http://resolver.tudelft.nl/uuid:e43683de-0270-46c4-b736-c3ddfe99736e>.
- [6] J.C. van Dijk, D.A. Wilms, *Water treatment without waste material-fundamentals and state of the art of pellet softening*, *J. Water Supply: Res. Technol.: AQUA* 40 (1991) 263–280.
- [7] M.J.A. Schetters, J.P. van der Hoek, O.J.I. Kramer, L.J. Kors, L.J. Palmen, B. Hofs, H. Koppers, Circular economy in drinking water treatment: re-use of ground pellets as seeding material in the pellet softening process, *Water Sci. Technol.* 71 (2015) 479–486, <https://doi.org/10.2166/wst.2014.494>.
- [8] C. Tang, B. Godsken, H. Aktor, M. van Rijn, J.B. Kristensen, P.S. Rosshaug, H. J. Albrechtsen, M. Rygaard, Procedure for calculating the calcium carbonate precipitation potential (CCPP) in drinking water supply: importance of temperature, ionic species and open/closed system, *Water* 13 (2020) 42, <https://doi.org/10.3390/w13010042>.
- [9] O.J.I. Kramer, P.J. de Moel, J.T. Padding, E.T. Baars, Y.M.F. el Hasadi, E.S. Boek, J. P. van der Hoek, Accurate voidage prediction in fluidisation systems for full-scale drinking water pellet softening reactors using data driven models, *J. Water Process. Eng.* 37 (2020) 1–15, <https://doi.org/10.1016/j.jwpe.2020.101481>.
- [10] C. van der Veen, A.J. Graveland, Central softening by crystallization in a fluidized-bed process, *J. Am. Water Works Assoc.* 80 (1988) 51–58, <https://doi.org/10.1002/j.1551-8833.1988.tb03053.x>.
- [11] World Health Organization, *Guidelines for Drinking-water Quality*, 4th edition, World Health Organization, 2017.
- [12] M. van Ammers, J.C. van Dijk, A.J. Graveland, P.A.N.M. Nühn, State of the art of pellet softening, in: *Water Supply: Proceedings of the Specialized Conference on New Technologies in Water Treatment*, Organized by the International Water Supply Association, Amsterdam, 15–19 September 1986, 1986, pp. 223–235.
- [13] K.M. van Schagen, Model-based Control of Drinking-water Treatment Plants, 2009. <http://repository.tudelft.nl/view/ir/uuid%3Afc4d865d-1ed7-409e-83ba-6270daced67/>.
- [14] S. Ergun, Fluid flow through packed columns, *Chem. Eng. Sci.* 48 (1952) 89–94.
- [15] P.C. Carman, Fluid flow through granular beds, *Trans. Inst. Chem. Eng.* 15 (1937) 32–48, [https://doi.org/10.1016/S0263-8762\(97\)80003-2](https://doi.org/10.1016/S0263-8762(97)80003-2).
- [16] K.M. van Schagen, L.C. Rietveld, R. Babuška, O.J.I. Kramer, Model-based operational constraints for fluidised bed crystallization, *Water Res.* 42 (2008) 327–337, <https://doi.org/10.1016/j.watres.2007.07.019>.
- [17] A.W.C. van der Helm, *Integrated Modeling of Ozonation for Optimization of Drinking Water Treatment*, Water Management Academic Press, Delft, 2007.
- [18] M. Groenendijk, T.S.C.M. van de Wetering, R. van Nieuwenhuijze, Central water softening: customer comfort is relevant in new WHO view, *Water Sci. Technol. Water Supply* 8 (2008) 69–74, <https://doi.org/10.2166/ws.2008.036>.
- [19] D.L. Boccelli, M.J. Small, U.M. Diwekar, Drinking water treatment plant design incorporating variability and uncertainty, *J. Environ. Eng.* 133 (2007) 303–312, [https://doi.org/10.1061/\(asce\)0733-9372\(2007\)133:3\(303\)](https://doi.org/10.1061/(asce)0733-9372(2007)133:3(303)).
- [20] Th.G. J. Bosklopper, L.C. Rietveld, R. Babuska, B. Smaal, J. Timmer, Integrated operation of drinking water treatment plant at Amsterdam water supply, *Water Sci. Technol. Water Supply* 4 (2004) 263–270, <https://doi.org/10.2166/ws.2004.0116>.
- [21] G. Instruments GmbH, Q.mOnixx – Smart Edge Device for Monitoring Applications, 2021. www.gantner-instruments.com.
- [22] G. Instruments GmbH, GL.bEnch – Data Acquisition Software, 2021. www.gantner-instruments.com.
- [23] NEN-EN 933-2, *Tests for Geometrical Properties of Aggregates - Part 2: Determination of Particle Size Distribution – Test Sieves, Nominal Sizes of Apertures*, Dutch Norm, ICS-code 91.100.15, 93.080.20, 2020.
- [24] T. Ferreira, W. Rasband, *ImageJ User Guide*, 2012, <https://doi.org/10.1038/nmeth.2019>.
- [25] *Retsch-Technology, Operating Instructions / Manual Particle Size Analysis System: Camsizer*, 2007.
- [26] P. Dirken, E.T. Baars, A.J. Graveland, C.F. Woensdregt, On the crystallization of calcite (CaCO₃) during the softening process of drinking water in a pellet reactor with fluidized beds of quartz, garnet and calcite seeds, in: *11th Symposium on Industrial Crystallization: Garmisch-Partenkirchen, Federal Republic of Germany September 18–20, 1990, 1990*, pp. 95–100.
- [27] L.G. Gibilaro, *Fluidization-dynamics, The Formulation and Applications of a Predictive Theory for the Fluidized State*, Butterworth-Heinemann, Oxford, 2001.
- [28] W.C. Yang, *Handbook of Fluidization and Fluid-particle Systems*, 1st ed., CRC Press, New-York, 2003 [https://doi.org/10.1016/S1672-2515\(07\)60126-2](https://doi.org/10.1016/S1672-2515(07)60126-2).
- [29] R. di Felice, Review article number 47: Of hydrodynamics of liquid fluidisation, *Chem. Eng. Sci.* 50 (1995) 1213–1245, [https://doi.org/10.1016/0009-2509\(95\)98838-6](https://doi.org/10.1016/0009-2509(95)98838-6).
- [30] R. di Felice, P.U. Foscolo, L.G. Gibilaro, The experimental determination of the force on spheres submerged in liquid interaction fluidized beds, *Chem. Eng. Process. Process. Intensif.* 25 (1989) 27–34, [https://doi.org/10.1016/0255-2701\(89\)85003-2](https://doi.org/10.1016/0255-2701(89)85003-2).
- [31] T.H. Nguyen, J.R. Grace, Forces on objects immersed in fluidized beds, *Powder Technol.* 19 (1978) 255–264, [https://doi.org/10.1016/0032-5910\(78\)80034-5](https://doi.org/10.1016/0032-5910(78)80034-5).
- [32] M.Jv. Goldschmidt, J.A.M. Kuipers, W.P.M. van Swaaij, Hydrodynamic modelling of dense gas-fluidised beds using the kinetic theory of granular flow: effect of coefficient of restitution on bed dynamics, *Chem. Eng. Sci.* 56 (2001) 571–578.
- [33] F. Cello, A. di Renzo, F.P. di Maio, A semi-empirical model for the drag force and fluid-particle interaction in polydisperse suspensions, *Chem. Eng. Sci.* 65 (2010) 2128–3139, <https://doi.org/10.1016/j.ces.2010.02.006>.
- [34] O.J.I. Kramer, J.T. Padding, W.H. van Vugt, P.J. de Moel, E.T. Baars, E.S. Boek, J. P. van der Hoek, Improvement of voidage prediction in liquid-solid fluidized beds by inclusion of the Froude number in effective drag relations, *Int. J. Multiph. Flow* 127 (2020), <https://doi.org/10.1016/j.ijmultiphaseflow.2020.103261>.
- [35] A. di Renzo, N. Grassano, F.P. di Maio, Force on a large sphere immersed in an expanded water-fluidized bed over a wide range of voidage values, *Powder Technol.* 316 (2017) 296–302, <https://doi.org/10.1016/j.powtec.2016.12.045>.
- [36] J.R. Grace, Contacting modes and behaviour classification of gas-solid and other two-phase suspensions, *Can. J. Chem. Eng.* 64 (1986) 353–363, <https://doi.org/10.1002/cjce.5450640301>.
- [37] K.E. Wirth, Fluid mechanics of circulating fluidized beds, *Chem. Eng. Technol.* 14 (1991) 29–38, <https://doi.org/10.1002/ceat.270140105>.
- [38] R.B. Bird, W.E. Stewart, E.N. Lightfoot, *Transport Phenomena, Revised, 2nd ed.*, John Wiley & Sons, Inc. International, New-York, 2007.
- [39] C.K. Gupta, D. Sathiyamoorthy, *Fluid Bed Technology in Materials Processing*, 1st ed., CRC Press LLC, Boca Raton, 1999. <http://books.google.com/books?id=pnwsQb1WPqWc&pgis=1>.
- [40] J.R. Koza, *Genetic Programming: On the Programming of Computers by Means of Natural Selection Complex Adaptive Systems*, 1992 papers2://publication/uuid/5DADD85F-EE2F-42E1-8BF8-2CC6959C4FA0.
- [41] O. Levenspiel, *Chemical Reaction Engineering*, 3rd ed., John Wiley & Sons, New York, 1999.
- [42] O.J.I. Kramer, P.J. de Moel, J.T. Padding, E.T. Baars, S.B. Rutten, A.H.E. Elarbab, J. F.M. Hooff, E.S. Boek, J.P. van der Hoek, New hydraulic insights into rapid sand filter bed backwashing using the Carman-Kozeny model, *Water Res.* 197 (2021) 1–11, <https://doi.org/10.1016/j.watres.2021.117085>.
- [43] D. Geldart, Types of gas fluidization, *Powder Technol.* 7 (1973) 285–292, [https://doi.org/10.1016/0032-5910\(73\)80037-3](https://doi.org/10.1016/0032-5910(73)80037-3).
- [44] J.M. Dallavalle, *Micromeritics – The Technology of Fine Particles*, 2nd ed., Pitman Publishing Ltd, London, 1948.
- [45] A.H. Dharmarajah, *Effect of Particle Shape on Prediction of Velocity-voidage Relationship in Fluidized Solid-liquid Systems*, 1982.
- [46] C.T. Crowe, F. Group, *Multiphase Flow Handbook*, 1st ed., CRC Press, New York, 2006.
- [47] A. di Renzo, F.P. di Maio, Homogeneous and bubbling fluidization regimes in DEM-CFD simulations: hydrodynamic stability of gas and liquid fluidized beds, *Chem. Eng. Sci.* 62 (2007) 116–130, <https://doi.org/10.1016/j.ces.2006.08.009>.
- [48] J.F. Richardson, W.N. Zaki, Sedimentation and fluidisation: part I, *Trans. Inst. Chem. Eng.* 32 (1954) 35–53, [https://doi.org/10.1016/S0263-8762\(97\)80006-8](https://doi.org/10.1016/S0263-8762(97)80006-8).
- [49] H.H. Ku, Notes on the use of propagation of error formulas, *J. Res. Natl. Bur. Stand. Sect. C Eng. Instrum.* 70C (1966) 263, <https://doi.org/10.6028/jres.070C.025>.
- [50] F. Hammes, N. Boon, M. Vital, P. Ross, A. Magic-Knezev, M. Dignum, Bacterial colonization of pellet softening reactors used during drinking water treatment, *Appl. Environ. Microbiol.* 77 (2011) 1041–1048, <https://doi.org/10.1128/AEM.02068-10>.